Crystal structure of Ni-sorbed synthetic vernadite: a powder X-ray diffraction study

S. Grangeon*, B. Lanson, M. Lanson and A. Manceau

Mineralogy and Environments Group, LGCA, Maison des Géosciences, BP53, Université Joseph Fourier − CNRS, 38041 Grenoble Cedex 9, France

ABSTRACT

Vernadite is a nanocrystalline turbostratic phyllomanganate containing Ni, and is widespread in surface environments and oceanic sediments. To improve our understanding of Ni uptake in this mineral, two series of analogues of vernadite (δ-MnO_2) were prepared with Ni/Mn atomic ratios of $0.002-0.105$ at pH4 and $0.002-0.177$ at pH 7. Their structures were characterized using X-ray powder diffraction (XRD). The δ-MnO_2 nano-crystals are essentially monolayers with coherent scattering domains sizes of ~10 Å perpendicular to the layering and ~55 Å within the layer plane. For Ni/Mn < 0.01, the layer charge deficit is apparently balanced entirely by interlayer Mn, Na and protons. At higher Ni/Mn, Ni occupies the same site as interlayer Mn above and below vacant sites within the MnO_2 layer and at sites along the edges of the layer. However, the layer charge is balanced differently at the two pH values. At pH 4, Ni uptake is accompanied by a reduction in structural Na and protons, whereas interlayer Mn remains strongly bound to the layers. At pH 7, interlayer Mn is less strongly bound and is partially replaced by Ni. The results of this study also suggest that the number of vacant octahedral sites and multi-valent charge-copmpensating interlayer species are underestimated by the currently used structure models of δ-MnO_2.

Introduction

The phyllomanganate vernadite, like its synthetic analogue δ-MnO_2 (McMurdie, 1944), is a nano-sized and turbostratic variety of birnessite which is a layered manganese oxide consisting of randomly stacked layers composed of MnO_6 octahedra (Bricker, 1965; Giovanoli, 1980). In the structure-model presently available for δ-MnO_2 (Villalobos *et al.*, 2006), the nano-sized layers contain only Mn^{4+} cations and vacant octahedral sites (6%), whose charge is compensated for by interlayer Na^+, ($Na_{0.24}(H_2O)_{0.72}$ $[Mn^{4+}_{0.94},\square_{0.06}]O_2$). Vernadite probably forms, at

least in part, from the biologically-mediated oxidation of Mn^{2+} (Tebo *et al.*, 2004). For example, different strains of fungi and bacteria have been shown to produce vernadite-like oxides (Mandernack *et al.*, 1995; Jurgensen *et al.*, 2004; Tebo *et al.*, 2004, 2005; Webb *et al.*, 2005; Miyata *et al.*, 2006; Villalobos *et al.*, 2006). Their high metal sorption capacities result from the combination of small particle size, which induces a large number of border sites, and of vacant layer sites, which create a locally strong charge deficit.

As a result of this reactivity, vernadite has a key influence on the mobility of metals in a variety of environments. For example, Ni and other trace metals were reported to be associated with vernadite-like minerals in oceanic and lake ferromanganese nodules and crusts (Aplin and Cronan, 1985; Bogdanov *et al.*, 1995; Koschinsky and Halbach, 1995; Lei and Boström, 1995; Exon

et al., 2002; Koschinsky and Hein, 2003; Bodeï *et al.*, 2007; Peacock and Sherman, 2007*a*; Manceau *et al.*, 2007*a*). Similarly, in Mn coatings deposited on water-processing filtration sands, Ni is essentially bound to vernadite (Manceau *et al.*, 2007*b*). Understanding the reactivity of vernadite with Ni and the stability of Ni-complexes requires gaining insights into the metal-mineral interactions occurring at the atomic scale. The usual diffraction methods, such as the Rietveld method, are impaired by the minute size and extreme stacking disorder of these compounds.

This article reports structure models for Ni-sorbed δ-MnO$_2$ using X-ray diffraction (XRD), and chemical data. The layer and interlayer crystal structure and the mean number of stacked layers were determined from the trial-and-error simulation of the *hk* scattering peaks and of the 00*l* reflections (Drits and Tchoubar, 1990; Plançon, 2002). This modelling approach was applied previously on synthetic and natural phyllomanganates differing in chemical composition and density of structural defects (Chukhrov *et al.*, 1985; Lanson *et al.*, 2000, 2002*a,b*, 2008; Gaillot *et al.*, 2003, 2005, 2007; Villalobos *et al.*, 2006). The validity of the structure models was assessed from the comparison with Ni-*K*-edge extended X-ray absorption fine structure (EXAFS) data and from bond valence calculations. Finally, structural mechanisms for the sorption of Ni onto δ-MnO$_2$ crystals are proposed from the integration of all results.

Experimental methods

Synthesis of δ-MnO$_2$ and Ni sorption protocol

The sample preparation was described previously (Manceau *et al.*, 2007*b*). Briefly, suspensions of Na-rich δ-MnO$_2$ were prepared following the protocol of Villalobos *et al.* (2003), kept hydrated for several days, and then equilibrated at pH 4 or pH 7 and enriched afterwards in Ni at constant pH by the slow (0.4 ml/min), dropwise addition of a 5×10^{-4} mol/l Ni(NO$_3$)$_2$ solution. After 12 h of equilibration, the suspensions were filtered, rinsed with a few ml of deionized water, and freeze-dried. The samples are named as in the previous study (Table 1).

Chemical analysis

The mean oxidation degree of Mn was determined by potentiometric titration using Mohr salt [(NH$_4$)$_2$Fe(SO$_4$)] and Na$_4$P$_2$O$_7$ (Lingane and Karplus, 1946; Vetter and Jaeger, 1966). Three measurements were made on each sample, and a reference was measured after each sample to ensure the absence of bias due to titrant ageing. Total Mn, Ni and Na contents were determined with a Perkin-Elmer Optima 3000 inductively coupled plasma-atomic emission spectrometer (ICP-AES) on aliquots of solutions prepared from ~5 mg powder digested in ~15 ml NH$_3$OHCl (0.7 mol/l, pH 1.9) for 1 min. The results are reported in Table 1.

TABLE 1. Chemical composition of Ni-sorbed δ-MnO$_2$ expressed as atomic ratios.

Sample	Na/Mn (%)	Ni/Mn (%)	Mn Ox.	Layer Mn^{3+}
NidBi2-4	18.39±0.30	0.23±0.23	3.74±0.03	0.09
NidBi11-4	16.99±0.27	1.07±0.23	3.73±0.03	n.d.
NidBi50-4	10.90±0.05	4.97±0.04	3.75±0.02	0.08
NidBi105-4	5.57±0.15	10.57±0.15	3.77±0.02	0.07
NidBi2-7	26.53±0.19	0.25±0.14	3.80±0.03	0.04
NidBi11-7	26.80±0.40	1.07±0.24	3.80±0.03	n.d.
NidBi56-7	20.87±0.22	5.66±0.15	3.85±0.02	0.01
NidBi177-7	7.61±0.22	17.78±0.21	3.94±0.01	0.00

Mn Ox. = 'oxidation degree'. Layer Mn^{3+} is calculated from the average oxidation degree of Mn and from the number of interlayer Mn atoms (Table 3), which are considered to be trivalent. Uncertainties in the mean values are calculated as the mean of standard errors (Webster, 2001). Sample names as in Manceau *et al.* (2007*b*).
n.d.: not determined.

X-ray diffraction

Powder X-ray diffraction patterns were recorded over the $5-80°2\theta$ angular range $(17.6-1.20$ Å$)$ with a $0.04°2\theta$ angular step and 40 s counting time per step, using a D5000 diffractometer equipped with a SolX solid-state detector from Baltic Scientific Instruments and Cu-$K\alpha$ radiation. Simulations were performed successively on the high- $(30-80°2\theta$ Cu-$K\alpha)$ and low- $(5-30°2\theta$ Cu-$K\alpha)$ angle regions of the XRD patterns. The high-angle region is dominated by the scattering from two-dimensional hk peaks, hkl reflections being unresolved owing to the random layer stacking (random rotations and/or translations in the $a-b$ plane are systematic between adjacent layers). The in-plane unit-cell parameters (a and b) were determined from the position of the peak at ~1.41 Å (31,02 peak using a C-centred unit-cell, in which a and b axes are orthogonal), which is little affected by other structural parameters. The unit-cell parameters relative to the layer stacking (c parameter, and α and β angles) and the space group were not determined because of the turbostratic stacking which leads to the absence of 3D periodicity. Despite the intrinsic structural disorder, atomic coordinates and site occupancies for layer (Mn) and interlayer (Na, Ni, Mn) cations were obtained from the simulation of the 11,20 peak (at ~2.42 Å), because its profile is strongly modulated by the crystal structure factor (Villalobos *et al.*, 2006; Drits *et al.*, 2007; Lanson *et al.*, 2008). The size of the coherent scattering domains (CSDs), which are supposed to have a disk-like shape in the $a-b$ plane, was also derived from the modelling of the 11,20 peak profile. The low-angle region, which contains $00l$ reflections, was used to verify the lamellar character of the samples and to calculate the size of the CSDs along the $c*$ direction (i.e. the mean number of layers stacked coherently) and the d_{001} basal distance.

For simulations of the diffraction patterns, the background was fitted linearly for the two angular ranges. The quality of fit was evaluated with the R_{wp} and GoF (Goodness of fit = R_{wp}^2/R_{exp}^2) parameters (Attfield *et al.*, 1988; Howard and Preston, 1989). The uncertainty on the different structure parameters could not be determined quantitatively because the trial-and-error approach, required by the turbostratic nature of the samples investigated, does not allow the calculation of a covariance matrix. However, the uncertainty on interlayer cation site occupancy can be estimated to ±1% from the comparison of experimental and calculated XRD patterns (Manceau *et al.*, 1997). Further qualitative assessment of uncertainties is provided by Villalobos *et al.* (2006) and Lanson *et al.* (2008) using sensitivity tests.

Results

Qualitative description of XRD profiles

The XRD patterns of Ni-sorbed δ-MnO$_2$ are typical of turbostratic birnessite-like crystals (Fig. 1; Drits *et al.*, 1997; Villalobos *et al.*, 2006). The peaks at ~7.6 Å and ~3.7 Å correspond to basal reflections 001 and 002, although they do not form a strictly rational series (Lanson *et al.*, 2008). The broad and asymmetric scattering maxima at ~2.42 Å, ~1.41 Å and ~1.22 Å were indexed as 11,20, 31,02 and 22,40 peaks respectively, using a C-centred unit-cell (Drits *et al.*, 1997, 2007; Webb *et al.*, 2005; Villalobos *et al.*, 2006; Lanson *et al.*, 2008). For all samples, the d spacings of the 11,20 and 31,02 peaks are in a ratio ~1.72 – close to $\sqrt{3}$, indicative of a hexagonal layer symmetry. The symmetry of the 31,02 peak profile also supports a layer unit-cell that is hexagonal. If the layer unit-cell were orthogonal, this peak would split into separate 31 and 02 peaks and would be asymmetrical (Drits *et al.*, 2007; Lanson *et al.*, 2008).

At first glance, all XRD patterns look similar, with the systematic presence of poorly-defined $00l$ reflections in the low-angle region, and of hk peaks exhibiting similar relative intensities in the high-angle region. Upon closer examination, it appears however that only NidBi2-4 and NidBi11-4, and NidBi2-7 and NidBi11-7, are statistically indistinguishable (Fig. 1). Therefore, in the following NidBi11-4 and NidBi11-7 are omitted. The $00l$ reflections are more intense at pH 7 than pH 4, and decrease with increasing Ni content for the pH 4 series. The broad hump at $50-55°2\theta$ becomes more pronounced as the Ni content increases in the two pH series (Fig. 1).

As shown by Drits *et al.* (2007), the modulations of the 11,20 peak can be interpreted in structural terms. Specifically, XRD data resemble computations performed assuming hexagonal layer symmetry and ~17% vacant layer sites capped by interlayer Mn$^{2+/3+}$ in triple-corner sharing position (*TC* linkage, Fig. 2). The above described 'hump' is indeed characteristic of a large number (>10%) of layer vacancies capped
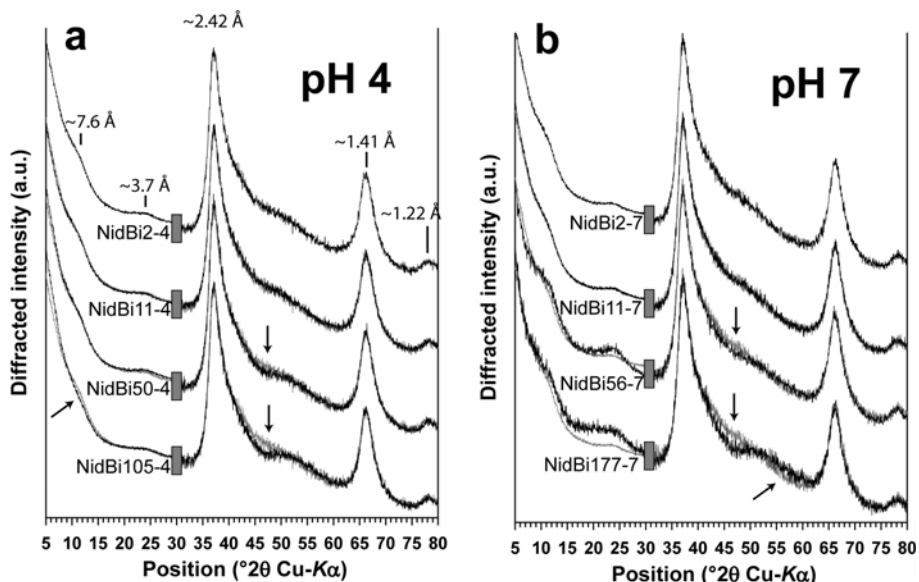
FIG. 1. XRD patterns of Ni-sorbed δ-MnO$_2$. (*a*) pH 4. (*b*) pH 7. The grey bar indicates a $5\times$ scale factor for the high-angle region except for samples NidBi56-7 and NidBi177-7 ($1.67\times$ scale factor). For each pH series, the sample with the lowest Ni/Mn ratio is systematically shown as a light grey line to emphasize the modification of XRD traces with Ni content (arrows).

by 'heavy' cations (fig. 13a,b in Drits *et al.*, 2007). Furthermore, 'heavy' interlayer cations are located mainly in *TC* rather than *TE* (triple edge sharing − Fig. 2) positions (see fig. 13c in Drits *et al.*, 2007). We can thus hypothesize, as a starting
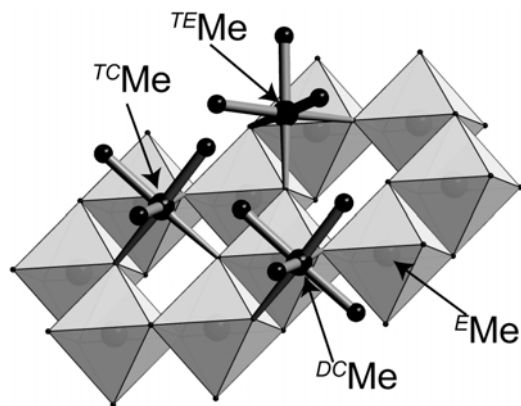

FIG. 2. Schematic representation of layer and interlayer sites reported in the literature for metal cations (including Mn) in δ-MnO$_2$. *TC*, *DC* and *TE* labels refer respectively to triple-corner sharing, double-corner sharing and triple-edge sharing sites. *E* label refers to layer sites.

model, that all Ni-sorbed δ-MnO$_2$ samples are turbostratic phyllomanganates whose layers have a hexagonal symmetry and bear significant amount of vacancies (>10%) capped mainly by 'heavy' interlayer species (Mn or Ni) in *TC* or *DC* sites.

Combining this tentative structure model and the chemical data reported in Table 1, the following generic structural formula can be proposed:

$$H_a^+Ni_b^{2+}Mn_c^{2+/3+}Na_d^+(H_2O)_e[Mn_f^{4+}Mn_g^{3+}Ni_h^{2+}\square_i]O_2$$
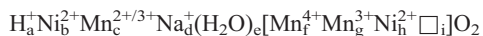
where species between square brackets are located within the octahedral layer ($\square$ stands for vacant layer sites) and those to the left of the brackets are interlayer species. The number of adjustable variables can be substantially reduced by physical and chemical constraints. First, EXAFS showed that Ni is predominantly located at *TC* and *DC* sites at pH 4 and pH 7 and Ni/Mn >1% (Manceau *et al.*, 2007b − <*d*(Ni−O)> ~2.05±0.02 Å). At a lesser Ni concentration, Ni partly fills vacant layer sites (*E* sites) in proportions which depend on the pH. This fraction was ignored in XRD simulations ($h = 0$) because it is minor (<1%) compared to the number of Mn atoms in the Mn layers, and because Mn and Ni have similar scattering factors. Interlayer Mn cations are octahedrally coordinated

TABLE 2. Crystal data for Ni-sorbed δ-MnO$_2$.

	NidBi2-4	NidBi50-4	NidBi105-4	NidBi2-7	NidBi56-7	NidBi177-7
a (Å)	4.916	4.912	4.910	4.917	4.919	4.917
b (Å)	2.838	2.836	2.835	2.839	2.840	2.839
d_{001} (Å)	7.3	7.3	7.3	7.3	7.3	7.3
Average CSD along $c*$ (Å)	11.0	10.2	9.5	12.4	15.3	11.0
CSD in the $a-b$ plane (Å)[a]	56	54	54	54	54	50
R_{wp} (%)[b]	5.72−6.32	4.12−5.17	4.97−5.00	8.74−6.15	5.22−5.82	5.21−6.06
GoF (%)[b]	6.49−4.53	3.57−3.32	5.41−3.33	15.40−4.45	8.42−6.52	5.41−4.17

[a] Diameter of the disk-like coherent scattering domains.
[b] First and second values are calculated over the low- and high-angle regions, respectively.

as is consistently reported in similar structures (Chukhrov *et al.*, 1985; Silvester *et al.*, 1997; Villalobos *et al.*, 2006; Lanson *et al.*, 2008). In the simulations, Na was coordinated to three water molecules as reported previously (Post and Veblen, 1990; Villalobos *et al.*, 2006). Finally, relative amounts of Mn^{4+}, Mn^{3+}, Ni^{2+}, and Na$^+$ were constrained to their chemical values (Table 1), and protons were eventually introduced to ensure the electro-neutrality of the structure. Parameters adjusted during the fitting process were thus limited to the distribution of Mn^{3+} cations between layer and interlayer sites, the position of interlayer Na$^+$ and coordinated H$_2$O molecules, and the coordinates of interlayer Mn, Ni, and associated H$_2$O molecules along the $c*$ axis.

Simulation of the high-angle (30−80°2θ Cu-Kα) region

In a first attempt, atomic coordinates were assumed to be identical for all samples, as the synthesis and sorption procedures were analogous, and only site occupancies were adjusted, together with unit-cell parameters and CSD sizes. Once the main features of all XRD patterns were satisfactorily reproduced, atomic coordinates were adjusted for each sample, but the fit to the data could not be improved significantly. Atomic positions are thus identical for all samples which differ only by their respective unit-cell parameters, CSD sizes, and their contents of the various interlayer species (Tables 2, 3). The best fits to the XRD data are shown in Fig. 3. The plausibility of the proposed models was assessed by calculating the valence of all atoms in the structure (Table 4 − Brown, 1996), which is an
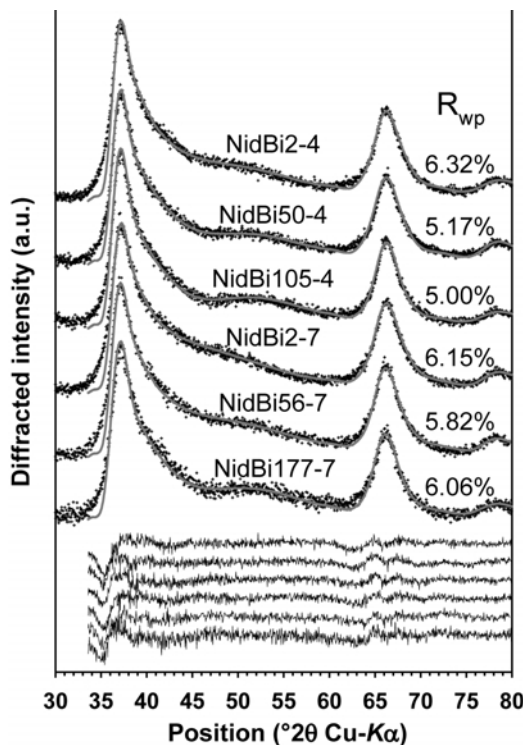

FIG. 3. Simulations of the 11,20, 31,02 and 22,40 X-ray scattering peaks (C-centred layer cell) for Ni-sorbed δ-MnO$_2$ samples. Black crosses are experimental data, solid grey overplots are calculated profiles, and solid lines at the bottom are difference plots. Structural parameters used for the simulations are listed in Tables 2 and 3.

TABLE 3. Structural parameters of Ni-sorbed δ-MnO$_2$ derived from XRD.

Atom	x[a]	y	z	ζ[b]	Occ.[c] NidBi2-4	Occ.[c] NidBi50-4	Occ.[c] NidBi105-4	Occ.[c] NidBi2-7	Occ.[c] NidBi56-7	Occ.[c] NidBi177-7
Mn$_{layer}$ (Mn1)	0.000	0.000	0.000	0.000	0.82	0.82	0.82	0.82	0.815	0.84
O$_{Mn1}$ (O1)	0.333	0.000	0.139	1.015	2.00	2.00	2.00	2.00	2.00	2.00
^{TC}Mn (Mn2)	0.000	0.000	0.299	2.183	0.14	0.16	0.16	0.10	0.085	0.07
H$_2$O$_{Mn2}$ (O2)	−0.333	0.000	0.472	3.446	0.42	0.48	0.48	0.30	0.255	0.21
^{TE}Mn (Mn3)	−0.333	0.000	0.299	2.183	0.03	0.00	0.00	0.05	0.04	0.00
H$_2$O$_{Mn3}$ (O3)	0.000	0.000	0.472	3.446	0.09	0.00	0.00	0.15	0.12	0.00
^{TC}Ni (Ni1)	0.000	0.000	0.306	2.234	0.00	0.04	0.07	0.00	0.05	0.13
H$_2$O$_{Ni1}$ (O4)	−0.333	0.000	0.486	3.548	0.00	0.12	0.21	0.00	0.15	0.39
^{TE}Ni (Ni2)	−0.333	0.000	0.315	2.300	0.00	0.02	0.02	0.00	0.00	0.02
H$_2$O$_{Ni2}$ (O5)	0.000	0.000	0.486	3.548	0.00	0.06	0.06	0.00	0.00	0.06
Na$_{interlayer}$ (Na)[d]	−0.525	0.000	0.500	3.650	0.18	0.06	0.06	0.24	0.18	0.06
H$_2$O$_{Na+}$ (O6)[e]	0.200	0.000	0.500	3.650	0.54	0.18	0.18	0.72	0.54	0.18

[a] Atomic coordinates x, y, z are expressed as fractions of the a, b and d_{001} parameters, respectively. Positions are given in the (x, 0, z) form. Equivalent positions are ($x + \frac{1}{2}$, $\frac{1}{2}$, z), because the unit cell is C-centred. Additional equivalent positions are (−x, 0, −z).
[b] Coordinates along the c^* axis, ζ, are expressed in Å to emphasize the thickness of layer and interlayer polyhedra.
[c] Occupancies are given per half formula unit as the sum of the occupancies for all equivalent positions.
[d] Additional symmetry operations: (−$x/2 - \frac{1}{2}$, $3x/2 + \frac{1}{2}$, z), and (−$x/2 - \frac{1}{2}$, −$3x/2 - \frac{1}{2}$, z).
[e] Additional symmetry operations: (−$x/2$, $3x/2$, z), and (−$x/2$, −$3x/2$, z).
Unrefined Debye-Waller thermal factors (B) are equal to 0.5 for Mn$_{layer}$, 1.0 for O$_{layer}$, interlayer Mn and Ni, 1.5 for H$_2$O molecules bound to interlayer Mn and Ni, and 2.0 for other interlayer species (alkali cations and H$_2$O molecules).

efficient way to constrain the model (Gaillot *et al.*, 2003).

The crystals are systematically nanosized (50−56 Å in diameter in the layer plane). Layers contain a significant amount (16−18.5%) of vacant sites, which are capped on one or two sides by octahedrally coordinated Mn^{3+} and/or Ni^{2+}, depending on the Ni/Mn loading and on the equilibration pH. Na$^+$ and H$^+$ compensate for the remainder of the negative layer charge. With increasing Ni loading, the number of Ni complexes increases at the expense of Na$^+$ and/or interlayer Mn, depending on the pH series. At pH 4, Ni preferentially replaces Na$^+$, the number of ^{TC}Mn remaining constant within error, whereas Ni replaces both Na$^+$, ^{TC}Mn, and ^{TE}Mn at pH 7.

Interlayer Mn^{3+} and Ni^{2+} are octahedrally coordinated and located either above/below vacant layer sites or in *TE* sites. Sodium is located in the interlayer mid-plane, coordinated to three water molecules at 2.30 Å, 2.89 Å and 2.95 Å (Fig. 4). The first distance is shorter than commonly observed (i.e. ~2.45 Å in Angeli *et al.*, 2000) but has already been reported in the literature (Brown, 1977). The prevalence of monolayers precludes oxygen atoms from adja-cent layers from providing bond valence to Na, and thus favours strong interactions with inter-layer H$_2$O molecules. The first coordination sphere of Na$^+$ is limited to ~3.0 Å, consistent with theoretical studies (Delville, 1992). However, the sum of bond valence with H$_2$O molecules (O6) and layer oxygen (O1) is insufficient to compensate fully the Na$^+$ charge (Table 4), as discussed in the following section. The position of H$_2$O molecules coordinated to interlayer Na$^+$ allows for the formation of strong H-bonds with layer oxygen atoms (O$_{layer}$), with d(H$_2$O−O$_{layer}$) = 2.71 Å.

To match the measured mean oxidation degree of Mn, Mn^{3+} cations have to be included in the octahedral layers, but the number of ^{E}Mn^{3+} remains limited, peaking at ~9% of layer octahedra for sample NidBi2-4 (Table 1). This small number is consistent with the hexagonal symmetry of the layer (Gaillot *et al.*, 2005, 2007; Manceau *et al.*, 2005). The in-plane b unit-cell parameter (2.835 Å ⩽ b ⩽ 4 2.840 Å) is similar to those reported previously for δ-MnO$_2$ (2.838 Å in Villalobos *et al.*, 2006). The sensitivity to this parameter was assessed with sample NidBi105-4 from the variation of R$_{wp}$ as a function of the b
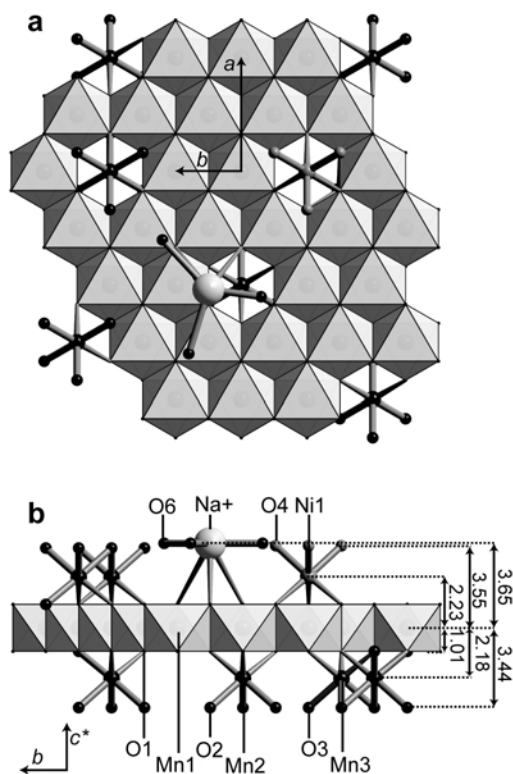
FIG. 4. Structure model of Ni-sorbed δ-MnO$_2$. (*a*) Projection on the *a*−*b* plane. (*b*) Projection on the *b*−*c** plane. Shaded octahedra represent layer Mn and its coordination sphere. Bonds between interlayer species and coordinating oxygens are shown in ball-and-stick. The distances of different atoms perpendicular to the layer of octahedrally-coordinated cations are given in Å.

parameter ($a = \sqrt{3} \times b$; Fig. 5). The estimated error on *b* is ±0.001 Å.

Simulation of the low-angle (5−30°2θ) region

The position, amplitude, and width of the two 00*l* reflections present over this low-angle region were simulated using the optimal structure models and adjusting only the out-of-plane d_{001} parameter and CSD size along the *c** direction. Experimental data were fitted with CSD sizes of 1.3 (9.5/7.3) to 2.1 (15.3/7.3) layers (Table 2, Fig. 6). Thus, most crystals consist of isolated layers. When a diffracting crystallite contains two or more layers, its layer stacking is random (i.e. turbostratic) as no significant modulations are
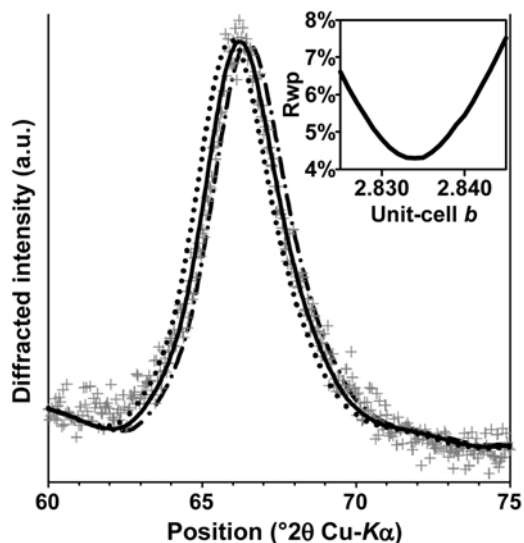

FIG. 5. Simulations of the 31,02 X-ray scattering peak (C-centred layer cell) for sample NidBi105-4. Grey crosses are experimental data, and lines are calculated profiles. The optimum fit to the data (solid line) was obtained with $b = 2.835$ Å and $a = \sqrt{3} \times b$ (Table 2). Varying *b* by ±0.01 Å with $a = \sqrt{3} \times b$ significantly decreases the fit quality. The inset shows the evolution of R$_{wp}$ with *b*.

visible on *hk* peaks (see Lanson *et al.*, 2008, for a discussion). The d_{001} basal distance determined (7.3 Å) is slightly greater than usually reported for both ordered and disordered birnessites (7.2 Å). This increased basal distance is consistent with the weak bonding between adjacent layers supported by the small CSD sizes.

Discussion

Composition of the interlayer

Except for Na, all atomic positions are consistent with those previously determined for metal-sorbed birnessite-like compounds, either well or poorly crystallized (Manceau *et al.*, 1997, 2002; Lanson *et al.*, 2002b, 2008; Villalobos *et al.*, 2006). The Na$^+$ position in Ni-sorbed δ-MnO$_2$ [(−0.525, 0, ½) and equivalent positions] contrasts with that reported previously for Na-bearing disordered birnessite [(−0.525, 0, ½) and equivalent positions − Villalobos *et al.*, 2006]. However, its coordination is similar in both cases with d(Na−O$_{layer}$) $\approx$ 2.66 Å. Na$^+$ coordination consists essentially of adjacent O$_{layer}$ atoms and
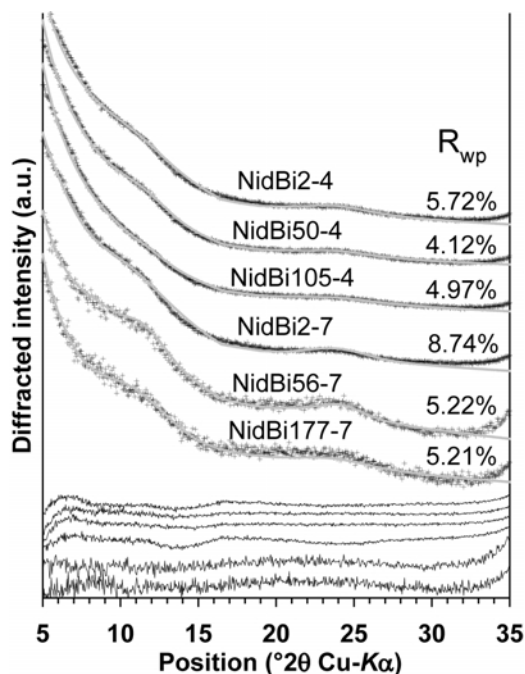
FIG. 6. Simulations of the 001 and 002 diffraction lines for Ni-sorbed δ-MnO₂. Patterns as in Fig. 4. Structural parameters used for the simulations are listed in Tables 2 and 3.

interlayer H_2O molecules, which, however, fail to compensate fully the charge of this cation (Table 4). The nanocrystalline character of δ-MnO₂, and specifically the prevalence of mono-layers, may account for the compensation of the remaining charge, as H_2O molecules hydrating the crystals may actually contribute to charge compensation. For crystals composed of more than one layer, O_{layer} from adjacent layers could also contribute to compensate the charge of interlayer Na, but sample turbostratism precludes the calculation of this bond valence.

The sensitivity of XRD patterns calculated for turbostratic birnessite to small variations of the site coordinates or occupancies has been discussed previously (Villalobos *et al.*, 2006; Drits *et al.*, 2007; Lanson *et al.*, 2008), and is not discussed further here in order to assess model robustness. The proposed structure model implies the replacement of interlayer Mn and Na cations by interlayer Ni (Table 3) with increasing Ni/Mn content. If based on XRD data only, this model could appear questionable, as XRD is sensitive only to the distribution of electronic density but

does not provide element-specific information. One could thus argue that XRD simulation demonstrates essentially an increase of the electronic density above/below vacant layer sites with increasing Ni/Mn content, especially for the pH 7 series. This modification of the electron density distribution could possibly result from a limited adsorption of Ni, assuming a constant number of interlayer Mn atoms. Various constraints allow rejection of this alternative structure model. First, the two elements do not have the same z coordinates, thus permitting their differentiation in the interlayer. Second, the mean oxidation degree of Mn increases with increasing Ni loading, showing that the amount of Mn^{3+}, which is dominantly present as an interlayer species, decreases with increasing Ni/Mn content. In addition, a Ni^{2+}-for-Na^+ exchange would lead to a strong excess of charge in the δ-MnO₂ structure, whereas the Ni^{2+}-for-Mn^{3+} exchange avoids this effect despite the increased number of interlayer cations above/below vacant layer sites. Finally, the evolution of the Ni/Mn ratio requires increase of the Ni content in the XRD simula-tions. EXAFS showed that Ni was not present as a precipitate (Manceau *et al.*, 2007*b*), that would probably also have been detected by XRD. The hypothesis of Ni sorption on the edges of δ-MnO₂ crystals at an octahedral layer site (*E* site; Fig. 2) may also be rejected as it would lead to a significant increase of the CSD size of these crystals within the *a*−*b* plane. The sorption of two Ni octahedra on the edges of δ-MnO₂ crystals would indeed increase the CSD size by 20−25% (from 54 to 66 Å in diameter), which would be easily detected by XRD owing to the high sensitivity of calculated patterns to this parameter (Villalobos *et al.*, 2006). In the case of NidBi105-4, such an increase of the CSD size would lead to R_{wp} and GoF values of 7.04% and 6.62, respectively, about twice the value of the optimal model (5.00%, and 3.33, respectively; Fig. 3). Such sorption would also affect the EXAFS signal, as edge-sharing Ni-Mn pairs are excluded at high Ni/Mn ratios (Manceau *et al.*, 2007*b*). Such an effect was not observed.

The local environment of Ni can be constrained further from Ni-EXAFS results obtained on the same samples by Manceau *et al.* (2007*b*). According to these results, Ni sorbs predomi-nantly as ^{TC}Ni and ^{DC}Ni complexes at pH 4−7 and Ni/Mn ratios >1%. The XRD and EXAFS models are therefore consistent, as the ^{TC}Ni and ^{DC}Ni sites are equivalent for XRD, the

TABLE 4. Bond valences calculated[a] for Ni-sorbed δ-MnO$_2$.

	O1[b]	O1[c]	O1[d]	O1[e]	O2/O3	O4/O5	O6	Σ	Formal valence
Mn1	0.625 × 6 → × 3↓			0.625 × 2↓				3.75	4
Mn2, Mn3		0.625 × 2↓ 0.509 × 3→	0.625 × 2↓		0.433 × 3→			2.8	3
Ni1, Ni2			0.298– 0.352[f] × 3→			0.300– 0.317[f] × 3→		1.9	2
Na^{+}				0.091 0.012 × 2→			0.261, 0.053, 0.045[g]	0.5	1
H^{+}			1.5–1.6[f]	0.105[h]	0.815 × 2↓	0.815 × 2↓	0.815 × 2↓		
Σ	1.9	1.8		1.3–1.4[I]	2.1	1.9	1.7–1.9[g]		

[a] Bond valences in valence units (v.u.) were calculated using the *VALENCE* for Dos program (v. 2.0 – http://www.ccp14.ac.uk/solution/bond_valence/index.html – Brown, 1996) and the parameters from Brese and O'Keeffe (1991).
[b] O1 coordinated to 3 Mn^{4+} in Mn1 (Table 3).
[c] O1 coordinated to 2 Mn^{4+} in Mn1 and 1 Mn^{3+} in Mn2 or Mn3 (Table 3).
[d] O1 coordinated to 2 Mn^{4+} in Mn1 and 1 Ni^{2+} in Ni1 or Ni2 (Table 3).
[e] O1 coordinated to 2 Mn^{4+} in Mn1 (Table 3).
[f] Depending on whether Ni is located in Ni1 or in Ni2.
[g] Na$^+$ is coordinated to 3 H$_2$O molecules at 2.30, 2.89, and 2.95 Å.
[h] O6–H–O1 H-bond.
[i] Depending on whether this O1 receives additional valence from Na$^+$ or from H$^+$ through H-bond.

investigated solids being too disordered to permit the discrimination of small differences in atomic coordinates. Despite the partial sorption of Ni at *DC* sites, i.e. on particle edges (Manceau *et al.*, 2007*b*), no increase of the CSD is observed. This observation is possibly due to the multiplicity of Ni sorption sites (*E*, *TC*, *DC*) and to the possibility for Ni atoms to sorb on the two *DC* sites on the same edge of the octahedron. Our results also agree with those reported by Peacock and Sherman (2007*b*) in their study of Ni sorption on synthetic hexagonal birnessite, a well crystallized phyllomanganate in which one sixth of the layer sites are vacant and capped by interlayer Mn^{3+} (Drits *et al.*, 1997; Silvester *et al.*, 1997; Lanson *et al.*, 2000). At pH 7, Peacock and Sherman (2007*b*) observed that ~90% of total Ni occupy *TC* sites. The apparent absence of ^{DC}Ni in their study is probably related to the larger lateral dimension of birnessite layers relative to δ-MnO_2 as the proportion of border sites, and thus surface reactivity of phyllomanganates in general, decreases considerbly when layer size increases (Tournassat *et al.*, 2002; Villalobos *et al.*, 2005; Webb *et al.*, 2005).

Sorption of metal cations at the *TE* site has only rarely been observed (Lanson *et al.*, 2002*b*, 2008). Here, it may be favoured by the combined effects of the high density of interlayer cations in the *TC* position and the probable presence of some layer Mn^{3+} cations (Table 1). Occupancy of the two *TC* positions induces electrostatic repulsion, especially when Ni^{2+} is facing a Mn^{3+} cation that can be minimized by moving one cation to the *TE* position. In addition, the combined presence of Mn^{3+} cations and of vacant sites in the octahedral layers results in the strong undersaturation of some O_{layer} atoms that is best compensated for by the presence of interlayer cations in both *TC* and *TE* sites (Lanson *et al.*, 2002*b*).

Ni sorption mechanism

Although similar structure models were obtained for the two δ-MnO_2 series, the mechanism of Ni sorption probably differs at the two pHs, as attested macroscopically by the twofold increase in the evolution of the mean Mn oxidation degree with Ni loading at pH 7 (Fig. 7). Chemical data and XRD simulations suggest that at pH 4, Ni^{2+} preferentially replaces Na^+ and H^+, Mn^{3+} being strongly bound to the octahedral layers, whereas Ni^{2+} more readily exchanges for Mn^{3+} at pH 7. This contrasting behaviour could result from the larger

number of Mn^{3+} cations in the octahedral layers at low pH. As discussed above, the coexistence in octahedral layers of vacant layer sites and Mn^{3+} cations induces a strong undersaturation of O_{layer} atoms and therefore favours the binding of high-charge interlayer cations such as Mn^{3+}.

Comparison to structure models previously reported for δ-MnO_2

The structure of δ-MnO_2 has long been controversial. This compound, now known to be analogous to vernadite and turbostratic birnessite, was first reported by McMurdie (1944), and described as poorly crystalline cryptomelane (McMurdie and Golovato, 1948). In contrast, Feitknecht and Marti (1945) suggested a lamellar structure similar to pyrochroïte. The structural analogy between δ-MnO_2 and birnessite was suggested by Giovanoli (1969, 1980), and a structure model was proposed recently by Villalobos *et al.* (2006) using XRD and EXAFS spectroscopy. Despite the availability of structure models, and the demonstrated potential for structure characterization (Drits *et al.*, 2007), δ-MnO_2 is commonly referred to as 'amorphous manganese oxide' or as 'hydrous manganese oxide − HMO' (Xu and Yang, 2003; Boonfueng *et al.*, 2005; Huang *et al.*, 2007) without precise comment on important structural parameters such as the origin of the layer charge (vacant layer sites *vs.* Mn^{3+} in the layers).

The structure model proposed here differs in three points from the model proposed by

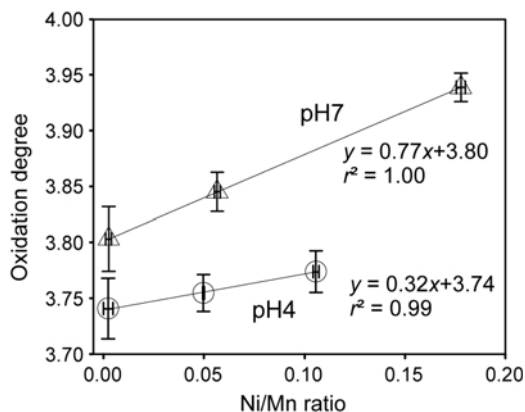FIG. 7. Average oxidation degree of Mn as a function of Ni/Mn ratio for Ni-sorbed δ-MnO_2 samples (circles: pH 4, triangles: pH 7).

Villalobos *et al.* (2006), who used another sample synthesized following the same protocol. Previously, the structure was considered to contain only Mn^{4+}, because the average oxidation degree obtained by the oxalate and iodine titration methods was 4.02±0.02 (see Villalobos *et al.*, 2003, for details). Here, a value of 3.80 ±0.03 has been measured at pH 7 and low Ni content (NidBi2-7), suggesting the presence of Mn^{3+} or Mn^{2+}. The presence of Mn^{3+} both within the octahedral layer and as interlayer species at *TC* and *TE* sites is supported by chemical, bond valence, and XRD results which consistently show that Mn^{2+} occurs only as a minor interlayer species, if present at all. In particular, the presence of Mn^{2+} at *TC* or *TE* sites is inconsistent with the coordination of interlayer Mn cations, determined from XRD modelling, requiring the mean Mn−O bond length to be ~0.15 Å longer than in the proposed structure model (Table 2). Although δ-MnO$_2$ was equilibrated at pH 8 in the previous study, the 0.2 difference in Mn mean oxidation state is probably experimental error because the oxalate and iodine methods used previously are less accurate than the Mohr salt/ sodium pyrophosphate method used in this study (Gaillot, 2002). This hypothesis was verified by re-measuring the original δ-MnO$_2$ sample (pH 8) studied by Villalobos *et al.* (2006) with the second titration method. A new value of 3.88 ±0.03 was obtained, consistent with the 3.80 ±0.03 value measured for NidBi2-7 taking into account the decrease in the mean oxidation degree of Mn with decreasing pH observed here and for soil Mn oxides (Negra *et al.*, 2005). Note also that the new model yielded a better fit to XRD data (R_{wp} = 6.2% and GoF ~ 4.6) than the previous model (R_{wp} = 10.7% and GoF ~ 9.4). The second difference, which derives directly from the smaller mean oxidation degree of Mn, is the presence of Mn^{3+} in the interlayer. Multivalent cations in *TC* and *TE* sites are more efficient at compensating the charge deficit of most under-saturated O_{layer} atoms than Na^+ and H^+ only, as was required in the previous model. The presence of multivalent cations at *TC* positions is also consistent with other structural studies on δ-MnO$_2$ and vernadite (Manceau *et al.*, 2007b; Peacock and Sherman, 2007b; Lanson *et al.*, 2008). Thirdly, the new model has 18% vacant layer sites, compared to 6% for the δ-MnO$_2$ sample studied previously. However, the new value does not reflect the actual number of vacant sites in the layer when CSDs are small in the *a*−*b* plane

(Webb *et al.*, 2005). Here, with a CSD size of ~55 Å, compared to ~120 Å previously, a large fraction of Ni atoms is sorbed on border sites as ^{DC}Ni complex when Ni/Mn >1% (Fig. 2). This complex increases the apparent number of layer vacancies seen by XRD because it has 2−3 nearest Mn neighbours instead of 6 for ^{TC}Ni on basal planes. Thus, the δ-MnO$_2$ crystals studied here have fewer layer vacancies than determined by XRD, because some of them are actually border sites. The distinction between interlayer and border sites becomes uncertain when crystals are vanishingly small.

Acknowledgements

References

Angeli, F., Delaye, J.M., Charpentier, T., Petit, J.C., Ghaleb, D. and Faucon, P. (2000) Influence of glass chemical composition on the Na-O bond distance: a ^{23}Na 3Q-MAS NMR and molecular dynamics study. *Journal of Non-Crystalline Solids*, **276**, 132−144.

Aplin, A.C. and Cronan, D.S. (1985) Ferromanganese oxide deposits from the Central Pacific Ocean, I. Encrustations from the Line Islands Archipelago. *Geochimica et Cosmochimica Acta*, **49**, 427−436.

Attfield, J.P., Cheetham, A.K., Cox, D.E. and Sleight, A.W. (1988) Synchrotron X-ray and neutron powder diffraction studies of the structure of α-CrPO$_4$. *Journal of Applied Crystallography*, **21**, 452−457.

Bodeï, S., Manceau, A., Geoffroy, N., Baronnet, A. and Buatier, M. (2007) Formation of todorokite from vernadite in Ni-rich hemipelagic sediments. *Geochimica et Cosmochimica Acta*, **71**, 5698−5716.

Bogdanov, Y.A., Gurvich, E.G., Bogdanova, O.Y., Ivanov, G.V., Isaeva, A.B., Murav'ev, K.G., Gorshkov, A.I. and Dubinina, G.I. (1995) Ferromanganese nodules of the Kara Sea. *Oceanology*, **34**, 722−732.

Boonfueng, T., Axe, L. and Xu, Y. (2005) Properties and structure of manganese oxide-coated clay. *Journal of Colloid and Interface Science*, **281**, 80−92.

Brese, N.E. and O'Keeffe, M. (1991) Bond-valence

parameters for solids. *Acta Crystallographica*, **B47**, 192−197.

Bricker, O. (1965) Some stability relations in the system Mn-O$_2$-H$_2$O at 25º and one atmosphere total pressure. *American Mineralogist*, **50**, 1296−1354.

Brown, I.D. (1977) Predicting bond lengths in inorganic crystals. *Acta Crystallographica B*, **33**, 1305−1310.

Brown, I.D. (1996) VALENCE: a program for calculating bond valences. *Journal of Applied Crystallography*, **29**, 479−480.

Chukhrov, F.V., Sakharov, B.A., Gorshkov, A.I., Drits, V.A. and Dikov, Y.P. (1985) Crystal structure of birnessite from the Pacific ocean. *International Geology Review*, **27**, 1082−1088.

Delville, A. (1992) Structure of liquids at a solid interface: an application to the swelling of clay by water. *Langmuir*, **8**, 1796−1805.

Drits, V.A. and Tchoubar, C. (1990) *X-ray Diffraction by Disordered Lamellar Structures: Theory and Applications to Microdivided Silicates and Carbons*. Springer-Verlag, Berlin, 371 pp.

Drits, V.A., Silvester, E., Gorshkov, A.I. and Manceau, A. (1997) Structure of synthetic monoclinic Na-rich birnessite and hexagonal birnessite. I. Results from X-ray diffraction and selected-area electron diffraction. *American Mineralogist*, **82**, 946−961.

Drits, V.A., Lanson, B. and Gaillot, A.-C. (2007) Birnessite polytype systematics and identification by powder X-ray diffraction. *American Mineralogist*, **92**, 771−788.

Exon, N.F., Raven, M.D. and De Carlo, E.H. (2002) Ferromanganese nodules and crusts from the Christmas Island region, Indian Ocean. *Marine Georesources & Geotechnology*, **20**, 275−297.

Feitknecht, W.M. and Marti, W. (1945) Über Manganite und künstlichen Braunstein. *Helvetica Chimica Acta*, **28**, 149−156.

Gaillot, A.-C. (2002) *Caractérisation structurale de la birnessite: Influence du protocole de synthèse*. Ph.D. thesis, Université Joseph Fourier - Grenoble I, Grenoble, France, 392 pp.

Gaillot, A.-C., Flot, D., Drits, V.A., Manceau, A., Burghammer, M. and Lanson, B. (2003) Structure of synthetic K-rich birnessite obtained by high-temperature decomposition of KMnO$_4$. I. Two-layer polytype from 800ºC experiments. *Chemistry of Materials*, **15**, 4666−4678.

Gaillot, A.-C., Lanson, B. and Drits, V.A. (2005) Structure of birnessite obtained from decomposition of permanganate under soft hydrothermal conditions. 1. Chemical and structural evolution as a function of temperature. *Chemistry of Materials*, **17**, 2959−2975.

Gaillot, A.-C., Drits, V.A., Manceau, A. and Lanson, B. (2007) Structure of the synthetic K-rich phyllomanganate birnessite obtained by high-temperature

decomposition of KMnO$_4$: Substructures of K-rich birnessite from 1000ºC experiment. *Microporous and Mesoporous Materials*, **98**, 267−282.

Giovanoli, R. (1969) A simplified scheme for polymorphism in the manganese dioxides. *Chimia*, **23**, 470−472.

Giovanoli, R. (1980) Vernadite is random-stacked birnessite. *Mineralia Deposita*, **15**, 251−253.

Howard, S.A. and Preston, K.D. (1989) Profile fitting of powder diffraction patterns. Pp. 217−275 in: *Modern Powder Diffraction* (D.L. Bish and J.E. Post, editors). Reviews in Mineralogy and Geochemistry, **20**. Mineralogical Society of America, Chantilly, Virginia, USA.

Huang, X., Yue, H., Attia, A. and Yang, Y. (2007) Preparation and Properties of Manganese Oxide/Carbon Composites by Reduction of Potassium Permanganate with Acetylene Black. *Journal of The Electrochemical Society*, **154**, A26−A33.

Jurgensen, A., Widmeyer, J.R., Gordon, R.A., Bendell-Young, L.I., Moore, M.M. and Crozier, E.D. (2004) The structure of the manganese oxide on the sheath of the bacterium *Leptothrix discophora*: An XAFS study. *American Mineralogist*, **89**, 1110−1118.

Koschinsky, A. and Halbach, P. (1995) Sequential leaching of marine ferromanganese precipitates: Genetic implications. *Geochimica et Cosmochimica Acta*, **59**, 5113−5132.

Koschinsky, A. and Hein, J.R. (2003) Uptake of elements from seawater by ferromanganese crusts: solid-phase associations and seawater speciation. *Marine Geology*, **198**, 331−351.

Lanson, B., Drits, V.A., Silvester, E. and Manceau, A. (2000) Structure of H-exchange hexagonal birnessite and its mechanism of formation from Na-rich monoclinic buserite at low pH. *American Mineralogist*, **85**, 826−838.

Lanson, B., Drits, V.A., Feng, Q. and Manceau, A. (2002*a*) Structure of synthetic Na-birnessite: Evidence for a triclinic one-layer unit cell. *American Mineralogist*, **87**, 1662−1671.

Lanson, B., Drits, V.A., Gaillot, A.-C., Silvester, E., Plancon, A. and Manceau, A. (2002*b*) Structure of heavy-metal sorbed birnessite: Part 1. Results from X-ray diffraction. *American Mineralogist*, **87**, 1631−1645.

Lanson, B., Marcus, M.A., Fakra, S., Panfili, F., Geoffroy, N. and Manceau, A. (2008) Formation of Zn-Ca phyllomanganate nanoparticles in grass roots. *Geochimica et Cosmochimica Acta*, **72**, 2478−2490.

Lei, G. and Boström, K. (1995) Mineralogical control on transition metal distributions in marine manganese nodules. *Marine Geology*, **123**, 253−261.

Lingane, J.J. and Karplus, R. (1946) New method for determination of manganese. *Industrial and Engineering Chemistry. Analytical Edition*, **18**,

191−194.

Manceau, A., Drits, V.A., Silvester, E., Bartoli, C. and Lanson, B. (1997) Structural mechanism of Co^{2+} oxidation by the phyllomanganate buserite. *American Mineralogist*, **82**, 1150−1175.

Manceau, A., Lanson, B. and Drits, V.A. (2002) Structure of heavy metal sorbed birnessite. Part III: Results from powder and polarized extended X-ray absorption fine structure spectroscopy. *Geochimica et Cosmochimica Acta*, **66**, 2639−2663.

Manceau, A., Tommaseo, C., Rihs, S., Geoffroy, N., Chateigner, D., Schlegel, M., Tisserand, D., Marcus, M.A., Tamura, N. and Chen, Z.-S. (2005) Natural speciation of Mn, Ni, and Zn at the micrometer scale in a clayey paddy soil using X-ray fluorescence, absorption, and diffraction. *Geochimica et Cosmochimica Acta*, **69**, 4007−4034.

Manceau, A., Kersten, M., Marcus, M.A., Geoffroy, N. and Granina, L. (2007a) Ba and Ni speciation in a nodule of binary Mn oxide phase composition from Lake Baikal. *Geochimica et Cosmochimica Acta*, **71**, 1967−1981.

Manceau, A., Lanson, M. and Geoffroy, N. (2007b) Natural speciation of Ni, Zn, Ba, and As in ferromanganese coatings on quartz using X-ray fluorescence, absorption, and diffraction. *Geochimica et Cosmochimica Acta*, **71**, 95−128.

Mandernack, K.W., Post, J. and Tebo, B.M. (1995) Manganese mineral formation by bacterial spores of the marine *Bacillus* strain SG-1: Evidence for the direct oxidation of Mn(II) to Mn(IV) . *Geochimica et Cosmochimica Acta*, **59**, 4393−4408.

McMurdie, H.F. (1944) Microscopic and diffraction studies on dry cells and their raw materials. *Transactions of the Electrochemical Society*, **86**, 313−326.

McMurdie, H.F. and Golovato E. (1948) Study of the Modifications of Manganese Dioxide. *Journal of Research of the National Institute of Standards and Technology*, **41**, 589−600.

Miyata, N., Maruo, K., Tani, Y., Tsuno, H., Seyama, H., Soma, M. and Iwahori, K. (2006) Production of biogenic manganese oxides by anamorphic Ascomycete fungi isolated from streambed pebbles. *Geomicrobiology Journal*, **23**, 63−73.

Negra, C., Ross, D.S. and Lanzirotti, A. (2005) Oxidizing behavior of soil manganese: interactions among abundance, oxidation state, and pH. *Soil Science Society of America Journal*, **69**, 87−95.

Peacock, C.L. and Sherman, D.M. (2007a) Crystal-chemistry of Ni in marine ferromanganese crusts and nodules. *American Mineralogist*, **92**, 1087−1092.

Peacock, C.L. and Sherman, D.M. (2007b) Sorption of Ni by birnessite: Equilibrium controls on Ni in seawater. *Chemical Geology*, **238**, 94−106.

Plançon, A. (2002) CALCIPOW: a program for calculating the diffraction by disordered lamellar structures. *Journal of Applied Crystallography*, **35**, 377.

Post, J.E. and Veblen, D.R. (1990) Crystal structure determinations of synthetic sodium, magnesium, and potassium birnessite using TEM and the Rietveld method. *American Mineralogist*, **75**, 477−489.

Silvester, E., Manceau, A. and Drits, V.A. (1997) Structure of synthetic monoclinic Na-rich birnessite and hexagonal birnessite. II. Results from chemical studies and EXAFS spectroscopy. *American Mineralogist*, **82**, 962−978.

Tebo, B.M., Bargar, J.R., Clement, B.G., Dick, G.J., Murray, K.J., Parker, D., Verity, R. and Webb, S.M. (2004) Biogenic Manganese Oxides: Properties and Mechanisms of Formation. *Annual Review of Earth and Planetary Sciences*, **32**, 287−328.

Tebo, B.M., Johnson, H.A., McCarthy, J.K. and Templeton, A.S. (2005) Geomicrobiology of manganese(II) oxidation. *Trends in Microbiology*, **13**, 421−428.

Tournassat, C., Charlet, L., Bosbach, D. and Manceau, A. (2002) Arsenic(III) oxidation by birnessite and precipitation of manganese(II) arsenate. *Environmental Science and Technology*, **36**, 493−500.

Vetter, K.J. and Jaeger, N. (1966) Potentialausbildung an der Mangandioxid-Elektrode als oxidelektrode mit nichtstochiometrischem oxid. *Electrochimica Acta*, **11**, 401−419.

Villalobos, M., Toner, B., Bargar, J. and Sposito, G. (2003) Characterization of the manganese oxide produced by *Pseudomonas putida* strain MnB1. *Geochimica et Cosmochimica Acta*, **67**, 2649−2662.

Villalobos, M., Bargar, J. and Sposito, G. (2005) Mechanisms of Pb(II) sorption on a biogenic manganese oxide. *Environmental Science & Technology*, **39**, 569−576.

Villalobos, M., Lanson, B., Manceau, A., Toner, B. and Sposito, G. (2006) Structural model for the biogenic Mn oxide produced by *Pseudomonas putida*. *American Mineralogist*, **91**, 489−502.

Webb, S.M., Tebo, B.M. and Bargar, J.R. (2005) Structural characterization of biogenic Mn oxides produced in seawater by the marine *Bacillus sp.* strain SG-1. *American Mineralogist*, **90**, 1342−1357.

Webster, R. (2001) Statistics to support soil research and their presentation. *European Journal of Soil Science*, **52**, 331−340.

Xu, J.J. and Yang, J. (2003) Nanostructured amorphous manganese oxide cryogel as a high-rate lithium intercalation host. *Electrochemistry Communications*, **5**, 230−235.